

The GUAPOS project: G31.41+0.31 Unbiased ALMA sPectral Observational Survey.

IV. Phosphorus-bearing molecules and their relation with shock tracers

F. Fontani^{1,2,3}, C. Mininni⁴, M.T. Beltrán¹, V.M. Rivilla⁵, L. Colzi⁵, I. Jiménez-Serra⁵, Á. López-Gallifa⁵, Á. Sánchez-Monge^{6,7}, and S. Viti^{8,9}

¹ INAF - Osservatorio Astrofisico di Arcetri, Largo E. Fermi 5, I-50125, Florence (Italy)
e-mail: francesco.fontani@inaf.it

² Centre for Astrochemical Studies, Max-Planck-Institute for Extraterrestrial Physics, Giessenbachstrasse 1, 85748 Garching, Germany

³ LERMA, Observatoire de Paris, PSL Research University, CNRS, Sorbonne Université, F-92190 Meudon (France)

⁴ INAF - Istituto di Astrofisica e Planetologia Spaziali, Via Fosso del Cavaliere 100, I-00133 Roma (Italy)

⁵ Centro de Astrobiología (CSIC-INTA), Ctra Ajalvir km 4, 28850, Torrejón de Ardoz, Madrid (Spain)

⁶ Institut de Ciències de l'Espai (ICE, CSIC), Can Magrans s/n, E-08193, Bellaterra, Barcelona, Spain

⁷ Institut d'Estudis Espacials de Catalunya (IEEC), Barcelona, Spain

⁸ Leiden Observatory, Leiden University, PO Box 9513, 2300 RA Leiden, The Netherlands

⁹ Department of Physics and Astronomy, University College London, Gower Street, London, WC1E 6BT, UK

Received XXX; accepted YYY

ABSTRACT

Context. The astrochemistry of the important biogenic element phosphorus (P) is still poorly understood, but observational evidence indicates that P-bearing molecules are likely associated with shocks.

Aims. We study P-bearing molecules, as well as some shock tracers, towards one of the chemically richest hot molecular core, G31.41+0.31, in the framework of the project "G31.41+0.31 Unbiased ALMA sPectral Observational Survey" (GUAPOS), observed with the Atacama Large Millimeter Array (ALMA).

Methods. We have observed the molecules PN, PO, SO, SO₂, SiO, and SiS, through their rotational lines in the spectral range 84.05–115.91 GHz, covered by the GUAPOS project.

Results. PN is clearly detected while PO is tentatively detected. The PN emission arises from two regions southwest of the hot core peak, "1" and "2", and is undetected or tentatively detected towards the hot core peak. The PN and SiO lines are very similar both in spatial emission morphology and spectral shape. Region "1" is in part overlapping with the hot core and it is warmer than region "2", which is well separated from the hot core and located along the outflows identified in previous studies. The SO, SO₂, and SiS emissions are also detected towards the PN emitting regions "1" and "2", but arise mostly from the hot core. Moreover, the column density ratio SiO/PN remains constant in regions "1" and "2", while SO/PN, SiS/PN, and SO₂/PN decrease by about an order of magnitude from region "1" to region "2", indicating that SiO and PN have a common origin even in regions with different physical conditions. The PO/PN ratio in region "2", where PO is tentatively detected, is $\sim 0.6 - 0.9$, in line with the predictions of pure shock models.

Conclusions. Our study firmly confirms previous observational evidence that PN emission is tightly associated with SiO and it is likely a product of shock-chemistry, as the lack of a clear detection of PN towards the hot-core allows to rule out relevant formation pathways in hot gas. We propose the PN emitting region "2" as a new astrophysical laboratory for shock-chemistry studies.

Key words. astrochemistry – line: identification – ISM: molecules – ISM: individual objects: G31.41+0.31 – stars: formation

1. Introduction

Hot molecular cores (HMCs) are the cradles of future high-mass stars ($M \geq 8M_{\odot}$) and rich stellar clusters, and represent the chemically richest environment in the local interstellar medium (Bisschop et al. 2007; Fontani et al. 2007; Belloche et al. 2013; Rivilla et al. 2017). In fact, many complex astronomical molecules (i.e. molecules with at least 6 atoms), including organic ones (COMs) such as dimethyl ether, ethanol, methyl cyanide, vinyl cyanide, and many others (McGuire 2018, 2022) have been detected for the first time towards the well-known HMCs Orion-KL (Genzel & Stutzki 1989) and Sgr B2 (e.g. Bonfand et al. 2019).

Such rich chemistry is triggered by several physical processes. First, HMCs typically harbour one or more deeply embedded protostars which heat up their surrounding molecular gas up to temperatures $T \geq 100$ K. In this warm environment, the molecules in the ice mantles of dust grains, formed in the early cold phase, sublime back in the gas-phase via thermal and non-thermal desorption (e.g. Garrod et al. 2022), and gas reactions not efficient at low temperature start to proceed and form new, more complex molecules (Garrod & Herbst 2006; Bonfand et al. 2019; Gieser et al. 2019; Barger & Garrod 2020). Second, collimated jets and molecular outflows from the protostar(s) can trigger local chemistry typical of shocked gas such as grain sputtering and non-equilibrium chemistry (Hollenback & McKee 1989;

Bachiller 1996; Tychoniec et al. 2021). Therefore, HMCs with a well-known physical structure are excellent astronomical laboratories to study astrochemistry in a variety of conditions.

In this framework, the project "G31.41+0.31 Unbiased ALMA sPectral Observational Survey (GUAPOS)" (Mininni et al. 2020) is aimed to observe the full 3mm spectral window accessible with the Atacama Large Millimeter Array (ALMA) towards the well-known HMC G31.41+0.31 (G31 hereafter), located at heliocentric distance of 3.75 kpc (Immer et al. 2019, please see Mininni et al. 2020 for a detailed description of the source). The unbiased survey allows us to observe many transitions of different species and to confirm (or discard) their detection in a robust way. The proper identification of the species and of all their transitions is important also for a proper derivation of physical parameters such as abundances and excitation temperatures, crucial to appropriately constrain the chemical models. The project has already provided important constraints on the formation/destruction routes of potential pre-biotic species such as the three isomers of $C_2H_4O_2$ (Mininni et al. 2020), peptide-like bond molecules (Colzi et al. 2021), and oxygen- and nitrogen-bearing COMs (Mininni et al. 2023; López-Gallifa et al. 2023). In this work, we focus our analysis on phosphorus-bearing molecules.

Phosphorus (P) is a basic ingredient for life as we know it. P-compounds are unique to form large biomolecules, thanks to their extreme structural stability and functional reactivity. For these reasons, it is a crucial component, in the form of phosphates, of nucleic acids (RNA and DNA), cellular membranes (phospholipids), and the adenosine triphosphate (ATP), the key molecule for the energy transfers in cells (see e.g. Macía 2005, Pasek et al. 2017). Despite its low Solar abundance relative to hydrogen ($P/H \sim 3 \times 10^{-7}$, Asplund et al. 2009) with respect to the other biogenic elements such as C, O and N, its abundance in living organisms is several orders of magnitude higher than the Solar one, for example up to $P/H \sim 10^{-3}$ in bacteria (e.g. Fagerbakke et al. 1996). Therefore, understanding what is the main source and reservoir of P in space, how its compounds form and evolve, how they are transformed and/or conserved in star-forming regions and, finally, delivered to planetary systems, is of huge importance in astrophysics.

P is believed to be mainly formed in massive stars by neutron capture on silicon (Si) in hydrostatic neon-burning shells in the pre supernova (SN) stage (e.g. Koo et al. 2013 and references therein), and also in explosive carbon- and neon-burning layers during SN explosions (Woosley & Weaver 1995). In the interstellar medium, it is less depleted than previously thought based on observations of P-bearing molecules obtained in massive star-forming regions and evolved stars (Rivilla et al. 2016; Ziurys et al. 2018). Despite this, a handful of P-bearing molecular species (eight in total, including the tentative detection of SiP) have been detected in the interstellar medium, and only three of them in star-forming regions, namely PO (Rivilla et al. 2016; Lefloch et al. 2016; Wurmser & Bergner 2022), PN (Ziurys 1987; Fontani et al. 2016; Rivilla et al. 2018; Bergner et al. 2022; Wurmser & Bergner 2022), and PO^+ (Rivilla et al. 2022). Single-dish observations and interferometric maps of PN and PO, the P-bearing molecules which are easier to detect in star-forming regions (Fontani et al. 2016; Mininni et al. 2018; Rivilla et al. 2016, 2018; Bergner et al. 2022; Wurmser & Bergner 2022), and evolved stars (Agúndez et al. 2007; De Beck et al. 2013; Ziurys et al. 2018), agree with the fact that PN and PO are likely derived from a solid phosphorus carrier, based on their spatial association with SiO emission, a tracer of protostellar

outflows and shocks (Lefloch et al. 2016; Mininni et al. 2018; Rivilla et al. 2018; Fontani et al. 2019; Bernal et al. 2021).

However, the reactions leading to the formation of PN and (especially) PO are far to be clear, even though some theoretical works start to determine the key reactions of the network of phosphorus (Fernández-Ruz et al. 2023). For example, Rivilla et al. (2020) proposed that to justify the observed abundances, the molecules should not be directly sputtered from the grains but be formed through gas-phase photochemistry induced by ultraviolet (UV) photons from the protostar in post-shocked gas. García de la Concepción et al. (2021) proposed that PO can be formed from atomic P reacting with OH, particularly efficient in warm environments, and Jiménez-Serra et al. (2018) also proposed mechanisms involving energetic processing. Moreover, Rivilla et al. (2020) and Bergner et al. (2022) found that PN and PO emission is co-spatial with low-velocity and not with high-velocity SiO and SO emission, further complicating the simple scenario of pure grain sputtering.

We study here the P-bearing molecules detected in GUAPOS together with other shock tracers: the Silicon-bearing molecules SiO and SiS, and the sulphur-bearing species SO and SO_2 . The analysis of the aforementioned sulphur- and silicon-bearing species is limited to the regions in the core where the emission of the phosphorus molecules is significant. The paper is structured as follows: in Sect. 2 we describe the observations and data reduction. In Sect. 3 we illustrate the observational results, that we discuss in Sect. 4. Conclusions and future perspectives are given in Sect. 5.

2. Observations and data reduction

Observations towards the HMC G31 were taken with ALMA during Cycle 5 (project 2017.1.00501.S, P.I.: M.T. Beltrán) obtaining an unbiased spectral survey in Band 3 from 84.05 GHz up to 115.91 GHz. The frequency resolution is 0.49 MHz, corresponding to a velocity resolution of $\sim 1.6 \text{ km s}^{-1}$ at 90 GHz. The final angular resolution is $1''.2$ ($\sim 4500 \text{ au}$). The primary beam is $\sim 68''$ at 84 GHz and $\sim 50''$ at 115 GHz. The pointing centre of the observations is R.A.(J2000)= $18^{\text{h}}47^{\text{m}}34''.312$ and Dec.(J2000)= $-01^{\circ}12'45''.9$. The uncertainty on the flux calibration is $\sim 5\%$. For more details on the data reduction (calibration, baseline subtraction, cleaning and line identification) we refer to Mininni et al. (2020). The spectral analysis has been performed with the MADRID DATA CUBE ANALYSIS (MADCUBA¹, Martín et al. 2019) software, and will be described in Sect. 3.3.

3. Results

3.1. Emission morphology

3.1.1. PN, PO and SiO

Figure 1 shows the map of PN $J = 2 - 1$ (panel (a)) integrated in the velocity range with emission above 3σ rms, namely 85.7–105.8 km s^{-1} . As reference, the systemic velocity of G31 is 96.5 km s^{-1} . The emission morphology is extended and located mostly towards two regions, both south of the hot core peak. The emission peak of the most intense one is offset by $-1''.6, -0''.9$ from the phase centre, corresponding to $\sim 6900 \text{ au}$. It is labelled as "1" in Fig. 1. The second one has a complex shape with multiple peaks. The main intensity peak is offset by $-3''.9, -3.$

¹ MADCUBA is a software developed in the Madrid Center of Astrobiology (INTA-CSIC) which enables to visualise and analyse single spectra and data cubes: <https://cab.inta-csic.es/madcuba/>.

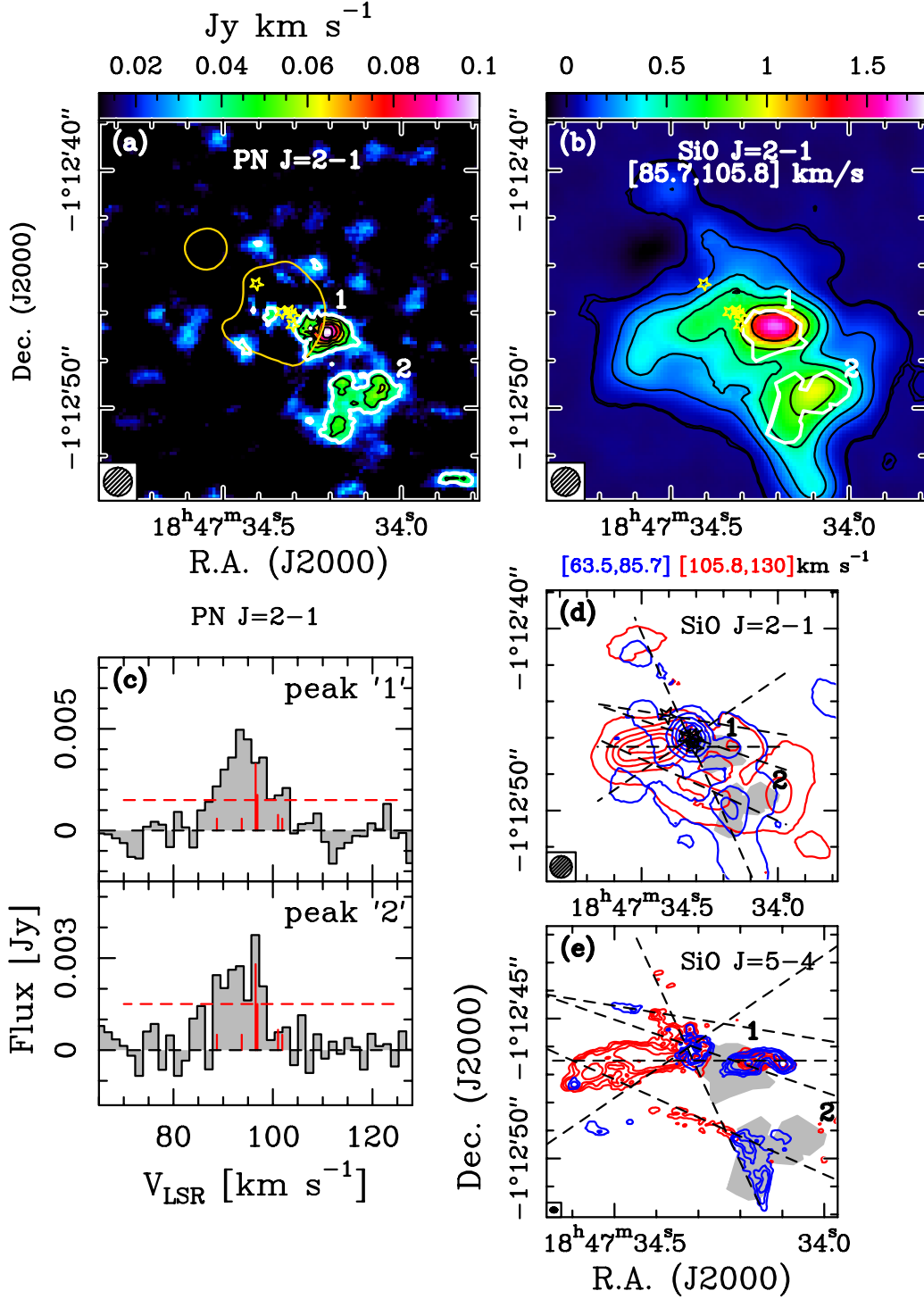


Fig. 1. Intensity maps of PN and SiO integrated in velocity.

(a): PN $J = 2 - 1$ integrated in the range 85.7–105.8 km s^{-1} . The white contour is the 3σ rms level of the integrated map ($\sigma = 1.14 \times 10^{-2}$ Jy km s^{-1}), while the black ones are in steps of 1σ rms. The numbered regions 1 and 2 are those used to extract the spectra of all species analysed. The synthesised beam is in the bottom-left corner. The yellow contour is the 3 mm continuum emission at 16 mJy beam^{-1} , corresponding to 20σ rms. The yellow stars indicate the continuum sources identified by Beltrán et al. (2021).

(b): map of the intensity of SiO $J = 2 - 1$ integrated in the same velocity range as PN (colour scale). The PN emission regions identified in panel (a) are highlighted in white. Contours start at the 3σ rms level of the integrated emission (3×10^{-2} Jy km s^{-1}), and correspond to 3, 15, 30, 50, 80, and 120σ .

(c): Spectra of PN $J = 2 - 1$ extracted from the emission peak in regions "1" (upper panel) and "2" (lower panel). The red dashed horizontal line indicates the 3σ rms level, and the vertical lines show the position in velocity of the line hyperfine components.

(d): SiO $J = 2 - 1$ emission integrated in the velocity ranges 63.5 – 85.7 km s^{-1} (blue contours) and 105.8 – 130.0 km s^{-1} (red contours). In both cases, the starting contour is the 3σ rms level of the integrated map (1.95×10^{-2} Jy km s^{-1} for the red contours, 1.62×10^{-2} Jy km s^{-1} for the blue contours), and the step is 25σ . The dashed lines correspond to the six outflows identified by Beltrán et al. (2022) from SiO $J = 5 - 4$. The grey filled areas correspond to the PN emitting regions 1 and 2 identified by Beltrán et al. (2022) from SiO $J = 5 - 4$.

(e): same as panel (d) for SiO $J = 5 - 4$, obtained at an angular resolution of $\sim 0.22''$ with ALMA, and already published in Beltrán et al. (2018). The integration velocity intervals are the same as in panel (d).

Table 1. Spectral parameters of the analysed transitions

Mol.	Transition	Rest Freq. (GHz)	$\log[A_{ij}]$ (s^{-1})	E_{up} (K)
PN	$N = 2 - 1, J = 2 - 2$	93.9782	-5.6144	6.8
	$N = 2 - 1, J = 1 - 0$	93.9785	-5.2677	6.8
	$N = 2 - 1, J = 2 - 1$	93.9798	-5.1373	6.8
	$N = 2 - 1, J = 3 - 2$	93.9799	-5.0123	6.8
	$N = 2 - 1, J = 1 - 2$	93.9808	-6.5687	6.8
	$N = 2 - 1, J = 1 - 1$	93.9823	-5.3926	6.8
PO	$J = 5/2 - 3/2,$ $\Omega = 1/2,$ $F = 3 - 2, l = e$	108.9984	-4.6712	8.4
	$F = 2 - 1, l = e$	109.0454	-4.7160	8.4
	$F = 3 - 2, l = f$	109.2062	-4.6689	8.4
	$F = 2 - 1, l = f$	109.2812	-4.7143	8.4
SiO	$J = 2 - 1$	86.8470	-4.5335	6.3
	$J = 5 - 4^a$	217.1050	-3.2843	31.3
^{29}SiO	$J = 2 - 1$	85.7592	-4.5500	6.2
SiS	$J = 5 - 4$	90.7716	-4.9241	13.1
	$J = 6 - 5$	108.9243	-4.6799	18.3
SO^b	$N = 2 - 1, J = 2 - 1$	86.0940	-5.2799	19.3
	$N = 3 - 2, J = 2 - 1$	99.2999	-4.9488	9.2
	$N = 4 - 4, J = 5 - 4$	100.0296	-5.9656	38.6
	$N = 2 - 1, J = 3 - 2$	109.2522	-4.9665	21.1
$^{34}\text{SO}^b$	$N = 2 - 1, J = 2 - 1$	84.4107	-5.30558	19.2
	$N = 4 - 4, J = 5 - 4$	96.7818	-6.0061	38.1
	$N = 3 - 2, J = 2 - 1$	97.7153	-4.9695	9.1
	$N = 2 - 1, J = 3 - 2$	106.7432	-4.9970	20.9
$^{33}\text{SO}^c$	$N = 2 - 1, J = 2 - 1$	85.2379	-5.2928	19.3
	$N = 3 - 2, J = 2 - 1$	98.4936	-4.9591	9.1
SO_2^d	$J_{K_a, K_b} = 3_{1,3} - 2_{0,2}$	104.0294	-4.2264	7.7
	$J_{K_a, K_b} = 16_{2,14} - 15_{3,13}$	104.0336	-5.4987	138
	$J_{K_a, K_b} = 10_{1,9} - 10_{0,10}$	104.2393	-3.7708	55

Notes. All parameters are taken from the Cologne Database for Molecular Spectroscopy (CDMS^a; Endres et al. 2016) ^(a) From observations in Beltrán et al. (2022); ^(b) For simplicity, in the text and figures we will label the SO and ^{34}SO transitions only with the N quantum number. We add the J of the upper level for the two transitions having the same N quantum numbers; ^(c) We list only the two (expected-to-be) strongest hyperfine transitions, $F = 7/2 - 5/2$ and $F = 9/2 - 7/2$. ^(d) We list only the lines detected towards the PN emitting regions.

^a <https://cdms.astro.uni-koeln.de/cdms/portal/>

"3 (corresponding to ~ 19000 au) from the phase centre, and is labelled region "2" in Fig. 1. Towards both peaks, we extracted the PN $J = 2 - 1$ spectra, which are shown in Fig. 1. The intensity of both lines is clearly above the 3σ rms level. PO is only tentatively detected towards G31, so that we do not show the integrated map here, and we refer to Sect. 3.2.2 for the analysis of this tentative detection.

Figure 1 also shows the emission of SiO $J = 2 - 1$ integrated in the same velocity range as PN $J = 2 - 1$ ($85.7 - 105.8$ km s⁻¹, panel (b)). The emission morphology is in very good agreement

with that of PN. In particular, SiO $J = 2 - 1$ does not peak on the hot core but towards the two PN emission regions. Evidence that PN and SiO are spatially associated was already found from both single-dish studies (Mininni et al. 2018; Rivilla et al. 2018; Fontani et al. 2019; Lefloch et al. 2016), and interferometric studies (Bergner et al. 2022). The maps in Fig. 1 confirm very clearly this association. The PN emission is less extended than that of SiO, perhaps due to insufficient sensitivity. To quantify this, first we have derived the contours at half maximum of the emission of PN and SiO in region "1". The contours subtend solid angles with equivalent diameters of $\sim 3''$ and $\sim 4''$, respectively. Hence, they are quite comparable. Second, we can quantify what the expected emission of PN would be in the envelope detected in SiO scaling the SiO integrated intensity by the PN/SiO abundance ratio. The average SiO integrated intensity in the envelope surrounding the emission peak "1" is ~ 0.4 Jy km s⁻¹. Multiplying this value by the lowest expected PN/SiO relative abundance, which is ~ 0.1 as we will show in Sect. 4.3, the integrated emission of PN would be $\sim 4 \times 10^{-2}$ Jy km s⁻¹, marginally higher than the 3σ rms level in the PN map that is 3.5×10^{-2} Jy km s⁻¹, and hence consistent with a non detection in PN.

Moreover, SiO is detected also at higher blue- and red-shifted velocities with respect to the velocities detected in PN. We show the integrated emission in the blue and red wings ($63.5 - 87$ km s⁻¹ and $102 - 130$ km s⁻¹, respectively) in panel (c) of Fig. 1. PN is undetected at these high velocities. However, the remarkable agreement between PN and SiO in the velocity range in which PN emission is significant, and where SiO emission is most intense, suggests that the two molecules have very similar emission structure.

In panel (d) of Fig. 1 we show the maps of the high-velocity wings of the SiO $J = 5 - 4$ line published in Beltrán et al. (2018). These maps have been obtained at an angular resolution of $\sim 0.22''$, that is ~ 5 times better than that of the GUAPOS ones. The orientation of the six outflows in the region and the position of their driving sources has been recently improved with ALMA ($\sim 0.09''$, Beltrán et al. 2022). We can see that the PN emission is entirely to the SW of the sources driving the outflows, and it can be associated with four of the six flows identified in Beltrán et al. (2022) at higher angular resolution. Thus, the complex PN emission we see in both regions "1" and "2" is probably due to the superposition of several outflow lobes. The superposition also suggests that PN seems to be mainly associated with the blue-shifted SiO outflow lobes (panel (d) in Fig. 1). In fact, even though region "1" is associated with both red-shifted and blue-shifted emission, region "2" is only detected in the blue-shifted emission. This could be due to the blue-shifted lobes being brighter compared to the red ones. Other reasons, such as inhomogeneity of the dense gas in the clump where the hot core (and outflows) are embedded, are also possible.

The PN emission is also clearly off the hot core location, and this result is consistent with what has been observed with ALMA in the young stellar objects AFGL5142 and B1 (Rivilla et al. 2020; Bergner et al. 2022). We checked if some PN emission arises also from the hot core analysing the spectrum extracted towards the 3 mm continuum (Mininni et al. 2020). The spectrum extracted from the 3 mm continuum contour surrounding the hot core (Fig. 1) is shown in Fig. 2. We chose the 3 mm continuum contour at 20σ rms to disentangle the emission of the hot core from that of the ultracompact HII region placed NE of the hot core (Mininni et al. 2020). We also show the spectrum extracted from a beam centred on the continuum intensity peak of the hot core. We detect a faint emission at ~ 100 km s⁻¹ and

$\sim 80 \text{ km s}^{-1}$ hence not centred on the systemic velocity of G31, which is 96.5 km s^{-1} . The feature at $\sim 100 \text{ km s}^{-1}$ is unlikely to be a nearby line because no other species have been found to emit lines at the frequency of this feature in previous GUAPOS works (Mininni et al. 2020; Colzi et al. 2021; López-Gallifa et al. 2023). Moreover, it is narrower (full width at half maximum $\sim 6 \text{ km s}^{-1}$) with respect to the lines detected towards the hot core, which have width at half maximum broader than 7 km s^{-1} (Mininni et al. 2020, 2023; Colzi et al. 2021). The hint of an absorption feature nearby (at $\sim 90 \text{ km s}^{-1}$) suggests that this could be PN partially self-absorbed. The fact that this absorption and emission features are both more prominent towards the total hot core than towards the peak could indicate that it is PN emission from the envelope, possibly associated with narrower features, and/or partially self-absorbed in the blue part of the line. However, the candidate absorption feature is too close to the noise level in both spectra, and hence we conclude that the emission from the hot core is lacking or negligible, as also suggested in López-Gallifa et al. (2023). The feature at $\sim 80 \text{ km s}^{-1}$ could be due to $n\text{-C}_3\text{H}_7\text{CN } 32_{5,28} - 32_{4,23}$ at 93.9839 GHz and/or $\text{gGg}'\text{-(CH}_2\text{OH)}_2 15_{1,14} - 14_{2,12}$ at 93.9818 GHz .

We stress that towards region "2" we identified all lines in the full GUAPOS spectrum, and found no lines of other identified species that could contaminate the PN $J = 2 - 1$ line. Moreover, all lines detected towards this region were identified. Towards region "1" the identification of all species is more difficult because the full spectrum is very rich of lines. However, the clean detection towards region "2" and the lack of candidate contaminating lines from other species towards the hot core (Fig. 2) makes a contamination from other lines in region "1" also unlikely. The identification of all species in regions "1" and "2", and their comparison, goes beyond the scope of this paper and will be the subject of a forthcoming work.

3.1.2. SO, SiS, and SO₂

Figure 3 shows the integrated intensity maps of the SO, SiS, and SO₂ transitions observed in GUAPOS and detected towards the PN emitting regions. The excitation analysis of all transitions of these species detected towards the hot core is performed in López-Gallifa et al. (2023). The SO emission arises mostly from the hot core, and shows some extended emission to the southwest, with a secondary peak towards the PN emitting region "2" clearly visible in transitions $N = 3 - 2$ and $N = 2 - 1(3)$. Hence, overall the bulk of SO emission has a different morphology with respect to both PN and SiO. The emission of both SiS and SO₂ is also dominated by the hot core, but there is a clear secondary peak coincident with region "2". The increase of the SO, SiS, and SO₂ integrated intensity towards the hot core is naturally explained if warm/hot gas-phase chemistry is boosting the formation of sulphur-bearing species. However, the SiS lines are also likely contaminated. In fact, SiS $J = 5 - 4$ is partly blended in the hot core with a line at 90.7697 GHz , unidentified so far, and the SiS $J = 6 - 5$ is blended with CH_3COCH_3 at 108.9237 GHz and to an unidentified line detected in the hot core at 108.9216 GHz . We will describe in Sect. 3.2 how such contaminations are clear in region "1", closer to the hot core, and disappear in region "2".

In summary, from the integrated intensity maps of all species the SiO emission is the most similar to the PN one. This is further illustrated in Fig. 4, where we plot the pixel-by-pixel ratio between the PN integrated intensity map and those of SiO $J = 2 - 1$, SiS $J = 5 - 4$, SO $N = 2 - 1(2)$, and SO₂ $J_{K_a, K_b} = 3_{1,3} - 2_{0,2}$. The ratio is nearly constant (within a factor two) for SiO/PN in

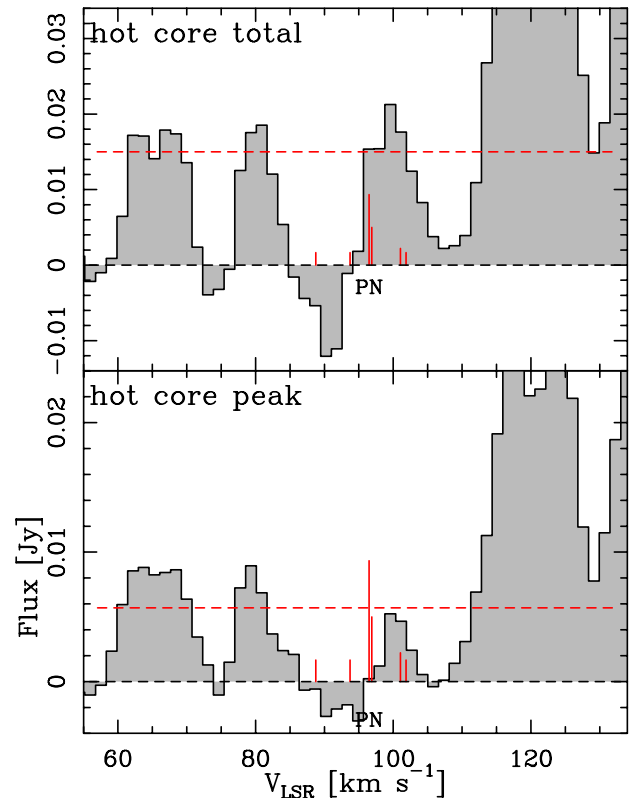


Fig. 2. Integrated PN $J = 2 - 1$ spectrum extracted from the hot core. The upper panel shows the spectrum extracted from the 3 mm continuum contour shown in Fig. 1. The lower panel shows the spectrum extracted from a beam around the intensity peak of the 3 mm continuum. The red vertical lines indicate the expected velocities of the hyperfine components, and their length is proportional to the relative intensity of the components. The horizontal lines illustrate the 3σ rms level.

both regions "1" and "2", while region "1" shows an increase up to a factor 10 of the ratios SiS/PN, SO/PN, and SO₂/PN towards the centre of the hot core. This shows further that both PN and SiO are formed predominantly in the outflows or in their cavities, while the Sulphur-bearing species are produced mostly in the hot core.

3.1.3. ²⁹SiO and ³⁴SO

Figure 5 shows the integrated intensity maps of the lines of the less abundant isotopologues clearly detected. Because these are expected to be optically thin, they should illustrate the actual morphology of the molecular emission better than their main isotopologues. The ²⁹SiO emission peaks on the hot core, contrary to the main isotopologue. However, this line is likely contaminated by two transitions: $\text{CH}_3\text{OCHO } 21_{5,16} - 21_{4,17}$ at 85.761876 GHz , and $\text{C}_2\text{H}_5\text{CN } J_{(K_1, K_2)} = 11_{2,10} - 11_{1,11}$ at 85.760502 GHz . The centroid velocity of this line is expected to be displaced by about -4.5 km s^{-1} from ²⁹SiO $J = 2 - 1$. Because both CH_3OCHO and $\text{C}_2\text{H}_5\text{CN}$ peak towards the hot core as the other COMs detected in the region, the fact that the emission peak in the map is on the hot core is likely due to this contamination.

The emission morphologies of the ³⁴SO lines are very similar to those of their main isotopologues: the $N = 3 - 2$ and $N = 2 - 1(3)$ transitions both peak towards the hot core but have a clear secondary peak towards the PN region "2". The $N = 2 - 1(2)$ line is mostly concentrated on the hot core and the

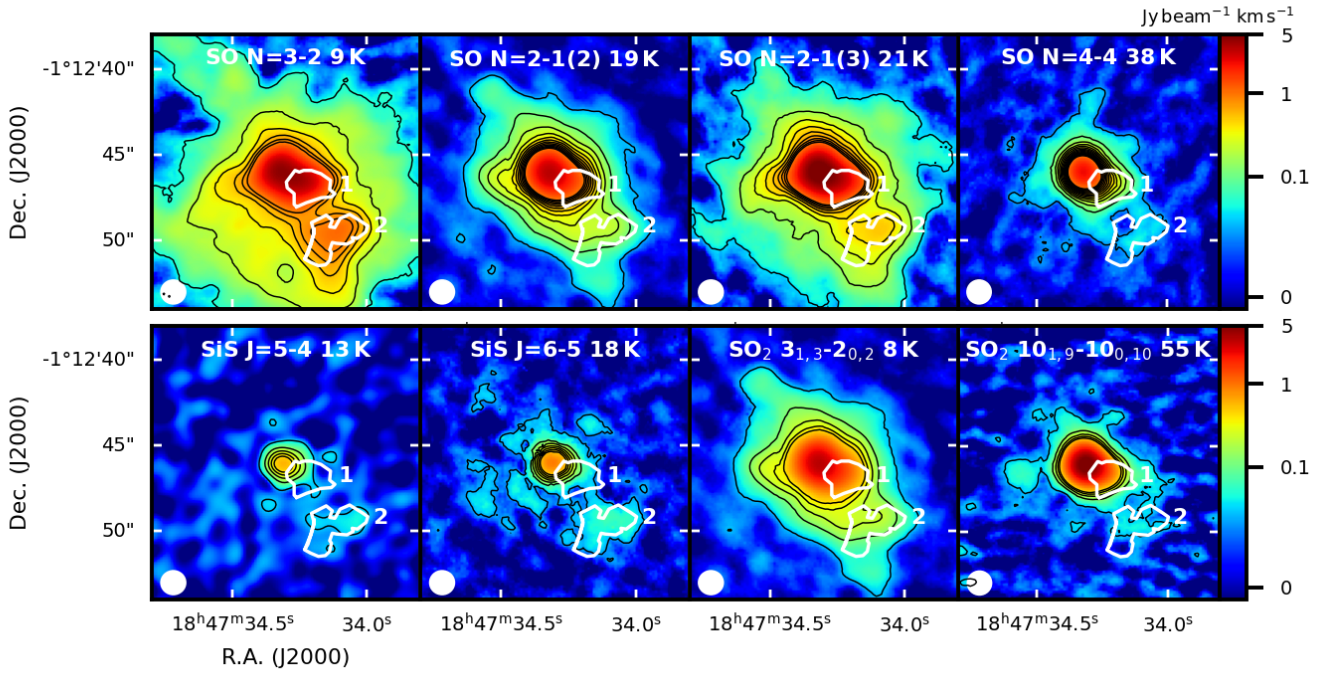


Fig. 3. Emission of SO, SiS, and SO₂ integrated in velocity. *Upper panels:* velocity-integrated emission of, from left to right, SO $N = 3 - 2$, $N = 2 - 1(2)$, $N = 2 - 1(3)$, and $N = 4 - 4$ (see Table 1 for the spectral parameters). The integration velocity range is 85.7–105.8 km s⁻¹ in all images to match the velocity interval where the PN emission is detected. The black contours start from the 3σ rms level of the integrated maps, which is, from left to right: 4.8×10^{-2} Jy beam⁻¹ km s⁻¹; 2.5×10^{-2} Jy beam⁻¹ km s⁻¹; 3.6×10^{-2} Jy beam⁻¹ km s⁻¹; 2.7×10^{-2} Jy beam⁻¹ km s⁻¹, and the step is of 10σ rms. The white contour corresponds to the PN integrated emission, and the numbered regions "1" and "2" are those defined in Fig. 1. The synthesised beam is illustrated in the lower-left corner. To the right of the quantum numbers, we indicate the E_{up} of the transition. *Lower panels:* same as the upper panels for the SiS $J = 5 - 4$ and $J = 6 - 5$ lines, and the SO₂ $J_{K_a, K_b} = 3_{1,3} - 2_{0,2}$ and $J_{K_a, K_b} = 10_{1,9} - 10_{0,10}$ lines. The 3σ rms level is: 2.9×10^{-2} Jy beam⁻¹ km s⁻¹ for SiS $J = 5 - 4$; 2.3×10^{-2} Jy beam⁻¹ km s⁻¹ for SiS $J = 6 - 5$; 2.95×10^{-3} Jy beam⁻¹ km s⁻¹ for SO₂ $J_{K_a, K_b} = 3_{1,3} - 3_{0,2}$; 1×10^{-2} Jy beam⁻¹ km s⁻¹ for SO₂ $J_{K_a, K_b} = 10_{1,9} - 10_{0,10}$.

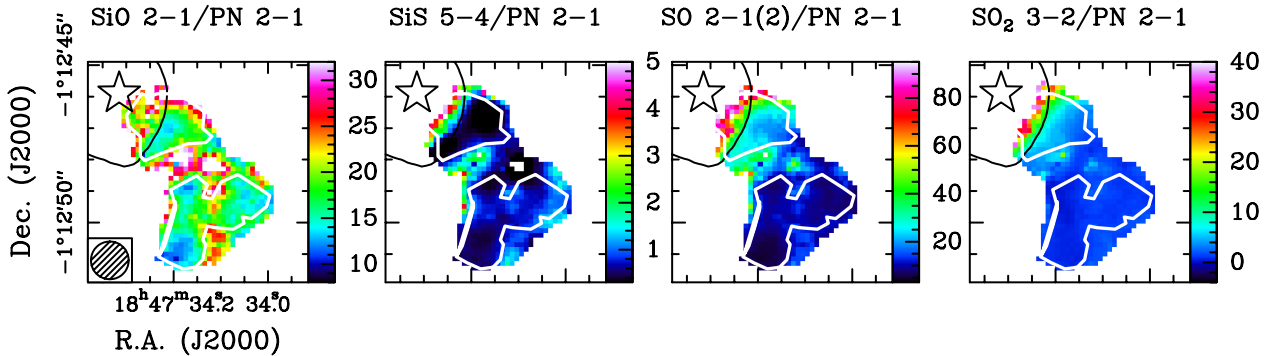


Fig. 4. Maps of integrated intensity ratios. The plots show the ratio between the PN integrated intensity and those of, from left to right: SiO $J = 2 - 1$, SiS $J = 5 - 4$, SO $J = 2 - 1(2)$, and SO₂ $J_{K_a, K_b} = 3_{1,3} - 2_{0,2}$. We show only the emission included, or close to, the two PN emitting regions "1" and "2", as the PN integrated emission goes rapidly to zero elsewhere. The star in the top left corner indicates the phase center, and the ellipse in the bottom left corner in the first panel is the GUAPOS synthesised beam. The black and white contours correspond to the 3 mm continuum emission and the PN integrated emission, respectively, as shown in Fig. 1.

secondary peak is barely visible, perhaps due to insufficient sensitivity. Therefore, the maps of the less abundant isotopologues of SO confirm the morphology of the main one, while that of SiO is different due to blending with a line arising from the hot core. We stress, however, that a possible partial contamination in region "1" is possible also in the ³⁴SO lines. In particular, the $N = 2 - 1(2)$ line could be contaminated by nearby lines of CH₃COOH and CH₃COCH₃ detected in the hot core. This would explain why the map of ³⁴SO in this line is more con-

centrated towards the hot core than the others. The $N = 3 - 2$ and $N = 2 - 1(3)$ could also be contaminated by nearby lines detected but unidentified in the hot core. Hence, in summary the analysis of all these lines towards region "1" should be regarded with caution due to strong contaminations.

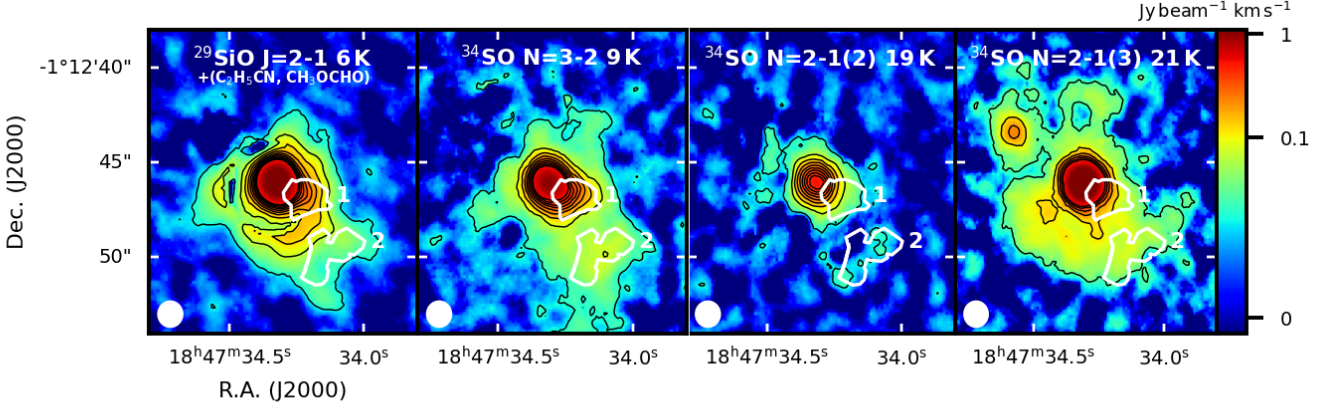


Fig. 5. Velocity-integrated emission of less abundant isotopologues. We show, from left to right, $^{29}\text{SiO } J = 2 - 1$, $^{34}\text{SO } N = 3 - 2$, $N = 2 - 1(2)$, and $N = 2 - 1(3)$. The integration velocity range is $85\text{--}101 \text{ km s}^{-1}$ for ^{29}SiO , which is the range in which PN and ^{29}SiO are both detected. For ^{34}SO , we have used: $81\text{--}105$ for the $N = 3 - 2$ line, $88\text{--}104 \text{ km s}^{-1}$ for the $N = 2 - 1(2)$ line, and $85.7\text{--}105.8 \text{ km s}^{-1}$ for the $N = 2 - 1(3)$ line. The black contours start at the 3σ rms level of the integrated intensity maps, which is, from left to right: $1.6 \times 10^{-2} \text{ Jy beam}^{-1} \text{ km s}^{-1}$; $1.8 \times 10^{-2} \text{ Jy beam}^{-1} \text{ km s}^{-1}$; $1.7 \times 10^{-2} \text{ Jy beam}^{-1} \text{ km s}^{-1}$; $8.7 \times 10^{-3} \text{ Jy beam}^{-1} \text{ km s}^{-1}$, and the step is 10σ rms. The white contour corresponds to the 3σ rms level of the integrated map of PN, and the numbered regions "1" and "2" are those defined in Fig. 1. The synthesised beam is illustrated in the bottom-left corner.

3.2. Spectra

3.2.1. Main isotopologues

In Figures 6 and 7 we show the spectra of the transitions of the main isotopologues reported in Table 1, extracted at the two emitting regions of PN $J = 2 - 1$ illustrated in Fig. 1. The spectra are in brightness temperature units. The conversion from flux density units to temperature units has been performed using Eq.(1) in Fontani et al. (2021), which provides an average brightness temperature over the angular surface of each region.

The spectral profiles of SiO and PN are compared in Fig. 8, and appear similar in both regions "1" and "2". This similarity is especially apparent in the central velocity channels, while it is less apparent at high velocities ($\geq 102 \text{ km s}^{-1}$, and $\leq 87 \text{ km s}^{-1}$), where the wings detected in SiO disappear in PN. This is likely due to insufficient sensitivity in this velocity range for PN. The detection of PN in a narrower velocity range with respect to SiO has also been found through ALMA observations in the high-mass protostar AFGL5142 (Rivilla et al. 2020) and the low-mass protostar B1-a (Bergner et al. 2022), as well as in single-dish studies (Lefloch et al. 2016; Mininni et al. 2018; Rivilla et al. 2018; Fontani et al. 2019).

Both SiS lines appear displaced (red-shifted) in velocity towards region "1" with respect to PN, SiO, and SO (Fig. 6). Such velocity shift is not seen in region "2", where the SiS velocity peak in both lines is placed very close to that of PN, SiO, and SO. We think that, in region "1", the SiS $J = 5 - 4$ line is contaminated by an unidentified line clearly detected towards the hot core at 90.7697 GHz , and the SiS $J = 6 - 5$ line is contaminated by emission of CH_3COCH_3 at 108.9237 GHz arising from the hot core, and by an unidentified line at 108.9216 GHz , both clearly detected towards the hot core (Mininni et al. 2023; Colzi et al. 2021).

The profiles of the SO transitions $N = 2 - 1(2)$ and $N = 3 - 2$ are, overall, similar to PN in region "1" (Fig. 7), even though the intensity peaks are slightly different: PN $J = 2 - 1$ and SO $N = 3 - 2$ peak at $\sim 94 \text{ km s}^{-1}$, while SO $N = 2 - 1(2)$ peaks at the G31 systemic velocity, that is 96.5 km s^{-1} . In region "2", the SO lines are narrower than those of PN and SiO, suggesting that SO can be dominated by more quiescent material, maybe

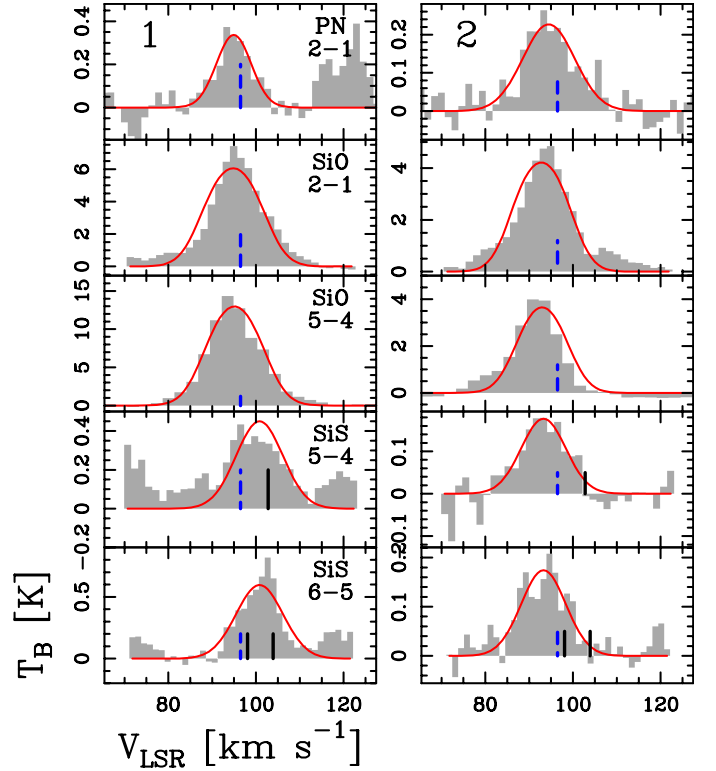


Fig. 6. Spectra extracted from the regions detected in PN $J = 2 - 1$. We show the transitions (from top to bottom) of PN ($J = 2 - 1$), SiO ($J = 2 - 1$ and $J = 5 - 4$), and SiS ($J = 5 - 4$ and $J = 6 - 5$). On top of each column we give the number of the extraction region according to the labels in Fig. 1. The blue dashed vertical lines correspond to the reference LSR velocity (96.5 km s^{-1} , Mininni et al. 2020). The black vertical lines in the panels of the SiS $J = 5 - 4$ line correspond to an unidentified line detected in the hot core at 90.7697 GHz , and in those of the $J = 6 - 5$ transition correspond to CH_3COCH_3 at 108.9237 GHz and to an unidentified line at 108.9216 GHz , both detected in the hot core (Mininni et al. 2023). The red curves superimposed on the lines represent the best LTE fit of the analysed molecules obtained with `MAF-CUBA`. For PN, we show the fit obtained fixing T_{ex} to that of SiO, that is 26 K (see Sect. 3.3.2).

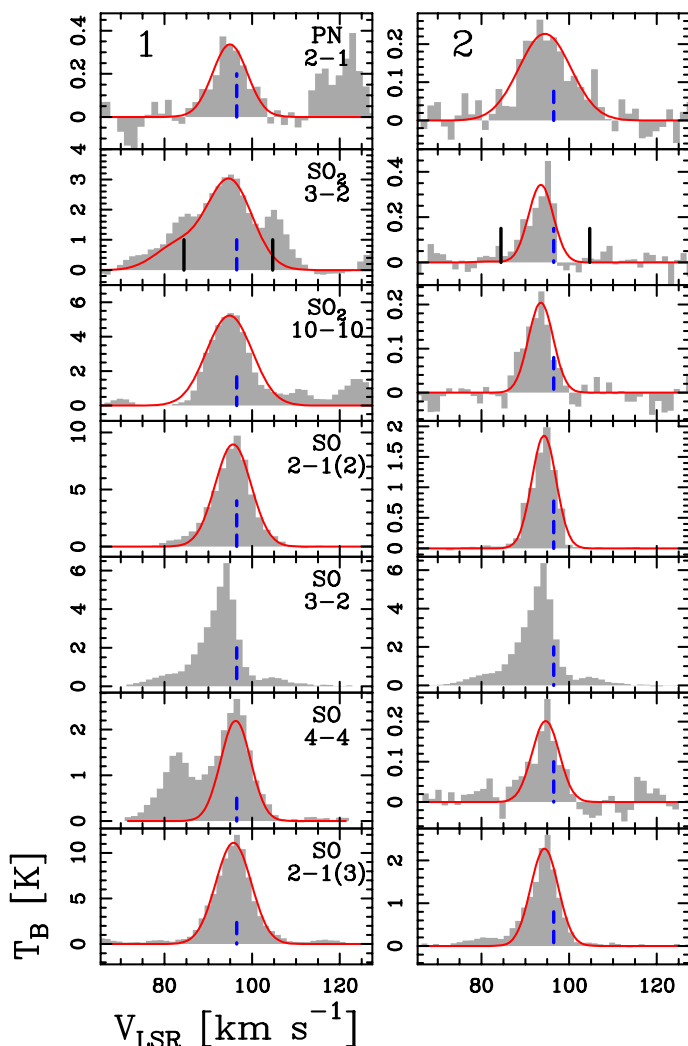


Fig. 7. Same as Fig. 6, showing the spectra of SO_2 ($J = 3 - 2$ and $J = 10 - 10$), and SO ($J = 2 - 1$, $J = 3 - 2$, and $J = 4 - 4$). We keep as reference the spectra of PN in the top panels as in Fig. 6. The black vertical lines in the spectrum of SO_2 $J = 3 - 2$ are SO_2 $J = 16 - 15$ (Table 1) and $^{13}\text{CH}_3\text{OH}$ $J = 13 - 14$ at 104.0266 GHz.

surrounding the outflow lobes, towards this position rather than by shocked material.

Finally, the SO_2 lines have a profile similar to that of SO in region "2", while in region "1" there are some differences: the $J_{K_a, K_b} = 10_{1,9} - 10_{0,10}$ transition has a profile similar to SO , while the $3_{1,3} - 2_{0,2}$ transition shows a blended profile with the SO_2 $16_{2,14} - 15_{3,13}$ line (undetected in region "2") and with $^{13}\text{CH}_3\text{OH}$ $13_{-3,11} - 14_{-2,13}$ at 104.02655 GHz, detected towards the hot core (Mininni et al. 2023) and not towards region "2".

3.2.2. Tentative detection of PO

The four lines of PO listed in Table 1 extracted from regions "1" and "2" are shown in the spectra of Fig. 9. We used *MADCUBA* to fit simultaneously the four transitions. The fitting method, which assumes local thermodynamic equilibrium (LTE) conditions, is fully described in Sect. 3.3.1. We have used the spectroscopic entry 047507 of the Cologne Database for Molecular Spectroscopy (CDMS), based on the laboratory measurements of Baillieux et al. (2002) and Kawaguchi et al. (1983), and the dipole moment determined by Kanata et al. (1988).

In region "1" (upper panel in Fig. 9), a detection of PO cannot be ruled out but it is difficult to claim due to the spectral complexity and the contamination by emission lines from other molecules (Fig. 9). In particular, the two PO transitions in the right panel of Fig. 9, namely the transitions at 109.2062 GHz and 109.2812 GHz, are blended with transitions of ethyl formate ($\text{C}_2\text{H}_5\text{OCHO}$) and ethylene glycol ($\text{aGg-CH}_2\text{OH}$)₂, respectively, as already found in source W51 (Rivilla et al. 2016). The lines contaminating the PO transitions in the left panel are not obvious to identify, as a proper determination of all contaminating species would require the study of the full GUAPOS spectrum towards this position. This goes beyond the scope of this paper and will be the subject of a forthcoming work.

In region "2" (lower panel in Fig. 9), less affected by nearby lines, the synthetic PO spectrum is consistent with a tentative detection. If we consider the peak intensity, the four transitions are below the 3σ rms noise, but if we consider the signal-to-noise ratio on the line integrated intensity, the two strongest transitions, that are at 108.9984 GHz and 109.2062 GHz, are consistent with a detection. The signal to noise ratio on the integrated intensity can be computed from the expression $\int T_B dV / [\sigma \times \sqrt{\Delta V / \text{FWHM}} \times \text{FWHM}]$, where ΔV is the spectral resolution in velocity. Plugging in this expression the line integrated intensity (0.51 K km s^{-1}), the 1σ rms (0.02 K), and the FWHM obtained with *MADCUBA* (12 km s^{-1} , see Table 2), we obtain a signal-to-noise ratio of ~ 6 . The spectrum towards this position was smoothed in velocity by a factor 2 to increase the sensitivity. The tentative detection is supported by the fact that the emission is most likely detected towards the two lines expected to be the strongest in the quadruplet (i.e. at 108.9984 GHz and 109.2062 GHz).

3.2.3. Less abundant isotopologues

The spectra of the less abundant isotopologues, namely ^{29}SiO , ^{34}SO , and ^{33}SO extracted from regions "1" and "2" are shown in Fig. 10. We detected clearly ^{29}SiO $J = 2 - 1$, ^{34}SO $N = 2 - 1(1)$, $3 - 2$ and $4 - 4$, in both regions. The detection of ^{34}SO $N = 2 - 1(2)$ and $4 - 4$ in region "2" is likely but difficult to firmly confirm because it is very close to the noise level. The line profiles of the ^{34}SO lines are overall similar in both line width at half maximum and centroid velocity to the corresponding ^{32}SO ones (compare Figs. 6 and 10).

The line profile of ^{29}SiO $J = 2 - 1$ is similar to the ^{28}SiO one in the red wing, but relatively much brighter than the ^{28}SiO one in the blue wing. As already noticed in Sect. 3.1.1, this excess emission is likely due to contamination from $\text{C}_2\text{H}_5\text{CN}$ emission, the expected centroid velocity of which is indicated in Fig. 10.

Figure 8 shows the PN $J = 2 - 1$ line profile superimposed on the detected lines of ^{29}SiO and ^{34}SO . For ^{34}SO , we use the two unblended lines $N = 2 - 1(2)$ and $N = 3 - 2$. In region "2", the PN and ^{29}SiO line profiles are very similar since ^{29}SiO is likely less blended. The ^{34}SO lines are very similar to PN in region "1", and narrower in region "2". As already noticed for the main isotopologue SO lines, this could be due to the fact that the SO emission is associated with a more quiescent material towards this position.

We did not clearly detect any ^{33}SO line, even though towards region "1" a tentative detection of the $J = 3 - 2$ transition is possible, as shown in Fig. 10. Assuming that the line is optically thin in both less abundant isotopologues, we can check if the tentative detection in ^{33}SO $N = 3 - 2$ is consistent with the expected line intensity: towards region "1" the $^{34}\text{S}/^{33}\text{S}$ ratio is ~ 5 . Because the

relative isotopic ratio $^{34}\text{S}/^{33}\text{S}$ is ~ 5.6 (Lodders 2003), the measured ratio is consistent with a tentative detection, but the ^{33}SO line also suffers from severe blending with nearby transitions, and hence we will not analyse it further.

3.3. Molecular column densities and excitation temperatures

In this section we derive the molecular column densities, N_{tot} , of the analysed species. We derive first N_{tot} and excitation temperature, T_{ex} , of the molecules detected in multiple lines, namely SO, ^{34}SO , SO_2 , SiS, and SiO (Sect 3.3.1). Then, using the excitation temperature derived from these species, we compute N_{tot} of PN and PO (Sect 3.3.2).

3.3.1. SO, ^{34}SO , SO_2 , SiS, and SiO

The fit to the spectra of SO, ^{34}SO , SO_2 , SiS, and SiO shown in Figs. 6, 7, and 10, and the derivation of the physical and spectral parameters has been performed with the Spectral Line Identification and LTE Modelling (SLIM) tool of MADCUBA. Through its AUTOFIT function, SLIM produces the synthetic spectrum that best matches the data assuming LTE. The input parameters are: T_{ex} , N_{tot} , radial velocity of the source (V), line full-width at half-maximum (FWHM), and angular size of the emission (θ_S). AUTOFIT assumes that V , FWHM, T_{ex} , and θ_S are the same for all transitions fitted simultaneously. These input parameters have all been left free except θ_S , for which we can safely assume that the emission fills the telescope beam, as can be seen in Figs. 3 and 5. The results are shown in Table 2.

Let us first present the best-fit parameters of the S-bearing species. For ^{34}SO , in region "1" the fit converged leaving V , FWHM, and N_{tot} free, but we had to fix T_{ex} . The best-fit T_{ex} obtained by visual inspection is 58 K. The resulting column density in region "1" is $\sim 1.1 \times 10^{15} \text{cm}^{-2}$. In region "2", the fit converged leaving all the parameters free, except the filling factor as explained above. The resulting N_{tot} is $\sim 8 \times 10^{13} \text{cm}^{-2}$, and T_{ex} is 25 K. For SO, in region "1" the fit could not converge leaving all parameters free and using all lines. Hence, first we did not use the $N = 3 - 2$ transition which has a spectral shape suggesting a (too) high optical depth. Then, we fitted the remaining three transitions fixing FWHM to 9km s^{-1} , which corresponds to the best-fit value derived from ^{34}SO . The resulting best-fit column density and T_{ex} are $1 \times 10^{16} \text{cm}^{-2}$ and 60 K, respectively. In region "2" the fit converged leaving all the parameters free, and the resulting column density and T_{ex} are $\sim 1.2 \times 10^{15} \text{cm}^{-2}$ and 31 K, respectively. The SO_2 excitation temperature in both regions is consistent within the uncertainties with the values measured from SO (~ 75 K in region "1" and ~ 27 K in region "2"), and the column densities are $\sim 9.8 \times 10^{15} \text{cm}^{-2}$ in region "1" and $\sim 1.6 \times 10^{14} \text{cm}^{-2}$ in region "2".

The fit of the lines of the Si-bearing species SiS and SiO (Fig.6) converged leaving all parameters free except the filling factor in both regions. However, as discussed in Sect. 3.2, the SiS lines in region "1" are both strongly blended with nearby lines, some of which are from unidentified species and hence could not be fitted simultaneously with SiS. Therefore, we derived N_{tot} and T_{ex} only for region "2", where we obtain $T_{\text{ex}} \sim 13$ K and $N_{\text{tot}} \sim 2.6 \times 10^{13} \text{cm}^{-2}$. For SiO, in region "1" we derive $T_{\text{ex}} \sim 26$ K and $N_{\text{tot}} \sim 3.6 \times 10^{14} \text{cm}^{-2}$, and in region "2" $T_{\text{ex}} \sim 12$ K and $N_{\text{tot}} \sim 1.8 \times 10^{14} \text{cm}^{-2}$. Finally, we did not estimate the parameters for ^{29}SiO because the line is too blended with a nearby line of $\text{C}_2\text{H}_5\text{CN}$, as discussed in Sect. 3.2.

3.3.2. PN and PO

For PN, we cannot derive T_{ex} from the data since we have only one transition. Hence, we derive the best-fit in a range of T_{ex} based on the minimum and maximum values obtained from the other tracers. These are: 26–75 K in region "1", and 12–30 K in region "2". The results are given in Table 2. The PN total column densities are of the order of 10^{13}cm^{-2} , regardless of the region and temperature assumed. The largest PN column density is measured towards region "1" assuming $T_{\text{ex}}=75$ K. We have fit the PN lines also taking the hyperfine structure into account, and derived in all cases FWHMs slightly smaller but consistent within the errors with the values obtained neglecting it.

For PO, as mentioned in Section 3.2.2, the PO transitions towards region "1" are significantly contaminated by brighter emission from other species. It was already noted by Rivilla et al. (2016) that the transitions at 109.2062 GHz and 109.2812 GHz are blended with transitions of ethyl formate ($\text{C}_2\text{H}_5\text{OCHO}$) and ethylene glycol ($\text{aGg-CH}_2\text{OH}$)₂, respectively. The contamination of the other two lines is less obvious and would require the analysis of the full GUAPOS spectrum towards this position, which is beyond the scope of this paper. Since the presence of PO in this position cannot be confirmed, we have thus derived an upper limit for its column density. We have used the values of T_{ex} , FWHM and V_{LSR} derived for PN, and using MADCUBA we have increased the value of N_{tot} to the maximum value that is consistent with the observing spectrum. The resulting LTE model is shown in Fig. 9, and the derived upper limit is $\sim 1.2 - 1.3$ (Table 2).

Regarding position "2", which is much less line-rich, the PO transitions are not contaminated, and they seem to be detected, especially the two brightest transitions. We have fitted them with MADCUBA, using again the same T_{ex} , FWHM and V_{LSR} derived for PN. The resulting LTE fit and N_{tot} are shown in Fig. 9, and Table 2, respectively. The PO/PN ratio turns out to be ≤ 1 , which is consistent with the results found in some low-mass star-forming regions (Wurmser & Bergner 2022), but smaller than the typical PO/PN ratios measured in high-mass star-forming regions (Rivilla et al. 2016, 2018) and in the comet 67P/Churyumov-Gerasimenko, where the PO/PN ratio is at least 10 (Rivilla et al. 2020).

3.3.3. Opacity of SiO and SO lines

MADCUBA estimates the line opacities as explained in Martín et al. (2019), and provides column densities already corrected for optical depth effects. The optical depth at the line centroid velocity, τ_{max} , computed with MADCUBA for each molecule is listed in Table 2. In case of multiple transitions, we list τ_{max} of the line having the highest opacity. The values shown in Table 2 indicate optically thin lines in most cases except SiO, for which τ_{max} is around 1, and SO, for which τ_{max} is ~ 0.3 .

For both SiO and SO lines, the opacity at line peak can also be computed from the less abundant isotopologues. Some lines of these isotopologues have the same quantum numbers as those of the main one (see Table 1). Hence, their excitation temperatures should also be comparable and the line opacity can be derived in an alternative way. If the emitting region is also the same for the two isotopologues, from the equation of radiative transfer one can demonstrate that the ratio between the line brightness temperature of two isotopologues depends only on their relative abundance, and on the optical depth of the main isotopologue. Let us consider the case of SiO: the line intensity ratio is given

Table 2. Best-fit spectral and physical parameters obtained with MADCUBA.

region	molecule	FWHM (km s ⁻¹)	<i>V</i> (km s ⁻¹)	<i>N</i> _{tot} (cm ⁻²)	<i>T</i> _{ex} (K)	τ_{\max}
"1"	³⁴ SO	9.0(0.9)	95.7(0.4)	1.1(0.1) × 10 ¹⁵	58	0.04
	SO	9.0	96.0(0.5)	1.0(0.2) × 10 ¹⁶	60(10)	0.34
	SO ₂	12.0(0.6)	94.8(0.3)	9.8(1.5) × 10 ¹⁵	75(10)	0.08
	SiS ^(a)	–	–	–	–	–
	SiO	12.6(0.4)	95.1(0.2)	3.6(0.1) × 10 ¹⁴	26.4(0.2)	0.9
	PN	9.7(0.9)	94.8(0.4)	1.3(0.1) × 10 ¹³	26	0.01
		9.7(0.9)	94.8(0.4)	3.1(0.3) × 10 ¹³	75	0.01
	PO	9.7	94.8	< 1.7 × 10 ¹³	26	–
	9.7	94.8	< 3.8 × 10 ¹³	75	–	
"2"	³⁴ SO	8.6(0.9)	93.8(0.4)	8(2) × 10 ¹³	25(10)	0.02
	SO	7.9(0.5)	94.8(0.4)	1.2(0.3) × 10 ¹⁵	31(12)	0.3
	SO ₂	6.2(0.6)	93.8(0.3)	1.6(0.2) × 10 ¹⁴	27(3)	0.02
	SiS	12.3(0.9)	93.3(0.4)	2.6(0.3) × 10 ¹³	13(1)	0.02
	SiO	11.5(0.6)	93.0(0.3)	1.8(0.2) × 10 ¹⁴	11.6(0.6)	0.7
	PN	11.7(1.2)	94.2(0.5)	1.5(0.1) × 10 ¹³	12	0.01
		12.2(1.2)	94.3(0.5)	1.6(0.1) × 10 ¹³	30	0.01
	PO	11.7	94.2	~ 8.5(1.4) × 10 ¹²	12	0.005
	12.2	94.3	~ 1.3(0.2) × 10 ¹³	30	< 0.001	

Notes. All parameters have been obtained with MADCUBA as described in Sect. 3.3.1. The numbers in brackets are the uncertainties. The quantities without uncertainties (in brackets) are fixed in the fit. ^(a) Both lines are strongly blended with nearby lines, some of which are from unidentified lines.

by

$$\frac{T_p^{28}}{T_p^{29}} \sim \frac{1 - \exp^{-\tau_{28}}}{1 - \exp^{-\tau_{28}/X[28/29]}} \quad (1)$$

where T_p^{28} and T_p^{29} are the brightness temperatures of the two lines, τ_{28} is the optical depth of the main isotopologue, and $X[28/29]$ is the ²⁸Si/²⁹Si relative abundance ratio. If $\tau_{28} \ll 1$, Eq.(1) states that $\frac{T_p^{28}}{T_p^{29}} \sim X[28/29]$, namely the temperature ratios should be equal to the expected isotopic ratio. For SO, an equation similar to Eq.(1) is valid for the ³²S/³⁴S and ³³S/³⁴S ratios.

The reference Solar values for ²⁸Si/²⁹Si and ³²SO/³⁴SO are 19.7 (Anders & Grevesse 1989) and 22.5 (Lodders 2003), respectively. Inspection of Fig. 8 shows that, at the velocity where the ²⁸SiO line peaks (i.e. ~ 94.8 km s⁻¹), the intensity ratio between the ²⁸SiO and the ²⁹SiO lines is ²⁸SiO/²⁹SiO ~ 8 in region "1" and ²⁸SiO/²⁹SiO ~ 20 in region "2". This indicates that in region "2", where the isotopic ratio is very close to the Solar one, both lines are likely optically thin. In region "1" the computed ²⁸SiO/²⁹SiO ratio gives $\tau_{28} \sim 2.35$, which is, however, an upper limit due to blending of ²⁹SiO with C₂H₅CN. In fact, the value computed by MADCUBA is $\tau_{28} \sim 1$. In region "2" MADCUBA provides $\tau_{28} \sim 0.7$, which is not consistent with optically thin lines, but at least with line opacity smaller than that in region "1".

The ³²SO/³⁴SO ratio derived from the $N = 2 - 1(1)$ line is ~ 22 in region "2", consistent with optically thin emission in both lines, and ³²SO/³⁴SO ~ 13 in region "1", smaller than the reference value by a factor 1.7. This ratio provides an optical depth $\tau_{32} \sim 1.2$ larger than the 0.34 value provided by MADCUBA, but still consistent with moderately optically thick lines. As stated in Sect. 3.3, the $N = 3 - 2$ line is more optically thick in region "1", but it has been excluded from the fit due to its complex spectral shape that did not allow the fit to converge.

4. Discussion

4.1. Comparison of spatial emission between PN and shock tracers

The most direct and apparent result of this study is the similar spatial distribution of PN and the SiO $J = 2 - 1$ bulk-velocity emission. This was already found in the intermediate-/high-mass protostellar object AFGL5142 (Rivilla et al. 2020), as well as in the low-mass protostar B1-a (Bergner et al. 2022) with ALMA observations. Our work agrees with the two mentioned works also in the fact that PN does not arise from the position of the protostar(s) embedded in the hot core. The non detection of PN towards the hot core could be explained either by insufficient atomic P to form PN, which in turn is abundant along the out-flow cavities owing to grain sputtering, or to disruption of the PN molecule in the high temperature and high irradiation environment of the hot core. However, other species sensitive to UV photodissociation, such as methanol, are abundant towards the hot core (Mininni et al. 2023). Jiménez-Serra et al. (2018) proposed that PH₃ is abundantly produced on grain surfaces via hydrogenation of P during the collapse phase. Then, upon evaporation, it is rapidly (in timescales of 10⁴ yrs) converted in PN and PO. However, both molecules are not detected clearly in the hot core, and hence PH₃ does not seem to be the main P-carrier here. The fact that PN is detected only in the shocked regions indicates that the main carrier of P is in the dust cores, where sputtering is needed to destroy (partially or totally) the grains.

The comparison between PN and SiS is less clear because the SiS emission is heavily contaminated by nearby lines close to the hot core. However, the PN line studied here has an energy of the upper level lower than those of the SiS lines ($E_{\text{up}} \sim 7$ K against $E_{\text{up}} \sim 13$ and ~ 18 K, respectively), and hence could be associated with (slightly) different material. If, and eventually how, the emission changes going to higher excitation lines needs to be investigated through maps of higher- J lines of PN.

At present, the map of PN at the highest J at high-angular resolution is the $J = 3 - 2$ one in Bergner et al. (2022), performed with ALMA towards B1-a. This map looks very similar in morphology to the PN $J = 2 - 1$ one obtained in the same work. However, the upper energy level of PN $J = 3 - 2$ is ~ 13.5 K, that is just a factor ≤ 2 higher than the $J = 2 - 1$ one. It would be hence interesting to map higher excitation PN lines to check if the intensity peak of the emission changes.

We also propose the PN emitting region "2" as a new "hot spot" for shocked material. Such region, well separated from the hot core, will allow us to study the chemistry of shocked gas without the influence of the hot core, similarly to other known chemically rich shocked protostellar spots like L1157–B1 (Gueth et al. 1998).

4.2. Comparison in velocity between PN and shock tracers

Another aspect emerging from our observations is the presence of PN only at relatively low velocities if compared with the velocities attained in the wings of the SiO and SO emission (see e.g. Fig. 6). This finding is, again, in agreement both with the high-angular resolution studies performed towards AFGL5241 and B1-a and with the single dish studies in Mininni et al. (2018) and Fontani et al. (2019). This could be due either to a lack of sensitivity in the high-velocity regime, or to the fact that PN is produced only in not-so-strong shocks. A similar behaviour is seen in young outflows (e.g. L1448-mm) where molecules such as H₂S fade away rapidly for high velocities while SiO and SO remain very bright at all velocities. One possibility could be the destruction of the onion-shell structure of dust grains where volatile species are detected at lower velocities due to the erosion of the ices and SiO and SO are also seen at high velocities because they are released from the grain cores (Jiménez-Serra et al. 2005). However, as discussed in Sect. 3.2.1, and also in Mininni et al. (2018) and Fontani et al. (2019), the fact that the line profile of PN and SiO is similar in the low(er) velocity channels suggests that the non-detection of PN at high velocities is more likely due to the lack of sensitivity.

To quantitatively establish this, we computed what the intensity in the wings of the SiO lines would be if the SiO abundance would be that of PN. The column density ratio PN/SiO is $\leq 1/10$ (Table 2). Fig. 6 indicates that the maximum intensity in the high-velocity wings of SiO $J = 2 - 1$ is ~ 1.5 K in region "1" and ~ 1 K in region "2". Scaling down these values by the abundance ratio PN/SiO $\sim 1/10$, which is reasonable because the emission in the wings is optically thin, one would obtain maximum intensities of 0.15 K and 0.1 K, respectively. The 1σ rms noise in the SiO $J = 2 - 1$ spectrum in region "1" is 0.1 K, and that in region "2" is 0.033 K. Thus, the intensities in the SiO wings scaled down by the PN/SiO factor would be at most 1.5 and 3 times the rms. Considering that these are upper limits, these results are consistent with a non-detection of the high-velocity wings, as we see in PN.

Concerning the PN peak velocity, in region "1" it is identical to the SiO one, and consistent within the uncertainties with those of SO, ³⁴SO, and SO₂. In region "2" the PN peak velocity is consistent within the uncertainties with that of all the other tracers except SiO, but the difference between the two values is just $\sim 1.2 - 1.3$ km s⁻¹, comparable to the velocity resolution of the observations.

4.3. Column density comparisons

Figure 11 shows the molecular total column density ratios between PN and the other species studied in this work. We plot the ratios for region "1" and "2" calculated assuming two T_{ex} as described in Sect. 3.3.2. The SO/PN, ³⁴SO/PN, and SO₂/PN ratios are higher in region "1" by about one order of magnitude than in region "2", while the SiO/PN ratios are consistent in the two regions within the uncertainties. Because N_{tot} of PN remains almost constant (around 10^{13} cm⁻²) in both "1" and "2", the different ratios between the two regions arise mostly from the decrease by an order of magnitude of N_{tot} of SO, ³⁴SO, and SiS. In Sect. 3.3.3, we evaluated that the SiO $J = 2 - 1$ line could be affected by optical depth towards region "1" possibly higher than that provided by MADCUBA. The upper limit on τ estimated this way is ~ 2.35 , instead of ~ 0.9 obtained with MADCUBA. Correcting N_{tot} in Table 2 for such different τ , one would obtain towards region "1" $N_{\text{tot}} \sim 6 \times 10^{14}$ cm⁻², and the SiO/PN ratios would become 66 and 24 for $T_{\text{ex}}[\text{PN}] = 12$ and 60 K, respectively. Even in this case the SiO/PN ratio for $T_{\text{ex}}[\text{PN}] = 12$ would be marginally consistent with the value in region "2".

The SO/PN ratio was found to vary by orders of magnitude in the protostar AFGL5142 (Rivilla et al. 2020). In the latter source, a high-mass protostar is driving a bipolar high-velocity jet surrounded by a cavity, both clearly detected in SO. Several emission spots of PN and PO were detected along the cavity walls, but they were both undetected towards the protostar and the jet. Towards the protostar and the jet, the SO/PN ratio was of the order of 1000 or more, similar to the value obtained in G31 towards region "1". Along the outflow *cavities*, instead, the SO/PN ratio drops down to $\sim 70 - 200$, consistent with the values we measure in region "2". As discussed in Sect. 3.3.3, the SO lines are affected by non-negligible opacities. In such case, the derived total column densities of SO could be lower limits, and so the SO/PN column density ratios should be even higher. The ³⁴SO/PN should not be affected by high optical depth effects, and even in this case the column density ratio drops by about an order of magnitude from region "1" to region "2". In summary, our study confirms that PN and SiO are very selective tracers of outflow cavities, unlike SO and SO₂.

Finally, the PO/PN ratio in region "2", where PO is tentatively detected, is $\sim 0.6 - 0.9$, and in region "1", the PO/PN upper limit is $\sim 1.2 - 1.3$, depending on the assumed temperature. These ratios, even though in line with previous measurements on low- and high-mass protostars (Rivilla et al. 2016; Lefloch et al. 2016; Wurmser & Bergner 2022), are lower than those obtained in the outflow spots of AFGL5142 (Rivilla et al. 2020), where PO/PN ≥ 1 and increasing with the distance from the protostar. Ratios PO/PN ≤ 1 are found in the theoretical models of Jiménez-Serra et al. (2018) in case of pure shock models, without the need of a high cosmic ray ionisation rate, which in turn would be needed to explain PO/PN > 1 .

5. Conclusions

In the context of the GUAPOS project, we have studied P-bearing molecules towards the HMC G31 at high-angular resolution to investigate their connection with shock chemistry.

- We have clearly detected the PN $J = 2 - 1$ transition and several SO, SO₂, SiO, and SiS rotational lines. PO lines are tentatively detected.
- The integrated intensity maps indicate that the emission of PN arises from two regions, "1" and "2", both southwest of

the hot core peak, where four of the six outflows detected in Beltrán et al. (2022) are placed. PN is not detected towards the hot core, even though region "1" is partly overlapping with it. This allows us to rule out important formation pathways in hot gas.

- The PN and SiO emissions are very similar in morphology and spectral shape, both having two strong emission peaks towards regions "1" and "2", while all sulphur bearing species emit predominantly from the hot core.
- We propose that the PN emitting region "2" is a "hot spot" for shocked material well separated from the hot core, that will allow us to study the chemistry of shocked gas without the influence of the hot core, similarly to other known chemically rich shocked regions powered by protostellar objects.
- We derive excitation temperatures in the range $\sim 26 - 75$ K in region "1", and in the range $\sim 12 - 30$ K in region "2". The column density ratios of all species with respect to that of PN decrease by about an order of magnitude from region "1" to "2", except the SiO/PN ratio, which is constant within the uncertainties in both regions further indicating a common origin of the two species.
- We derive a (tentative) column density ratio PO/PN ~ 1 in region "2", in line with a pure shock model that does not need high cosmic ray ionisation rates.

An interesting follow up of our study will be to map transitions of PN at higher excitation to test whether these lines trace different (e.g. innermost?) material. Moreover, observing more PN lines will allow us to derive T_{ex} for PN as well, and hence compute a more accurate estimate of N_{tot} .

Acknowledgements. We thank the anonymous referee for their careful reading of the article and their useful comments. C.M. acknowledges funding from the European Research Council (ERC) under the European Union's Horizon 2020 program, through the ECOGAL Synergy grant (grant ID 855130). V.M.R. has received support from the project RYC2020-029387-I funded by MCIN/AEI/10.13039/501100011033, and from the the Consejo Superior de Investigaciones Científicas (CSIC) and the Centro de Astrobiología (CAB) through the project 20225AT015 (Proyectos intramurales especiales del CSIC). I.J.-S. and L.C. acknowledge financial support through the Spanish grant PID2019-105552RB-C41 funded by MCIN/AEI/10.13039/501100011033. I.J.-S., L.C. and V.M.R. acknowledge also financial support through the Spanish grant PID2022-136814NBI00 funded by MCIN/AEI/10.13039/501100011033 and by "ERDF A way of making Europe". S.V. acknowledges support from the European Research Council (ERC) Advanced grant MOPPEX 833460. This paper makes use of the following ALMA data: ADS/JAO.ALMA#2013.1.00489.S and ADS/JAO.ALMA#2017.1.00501.S. ALMA is a partnership of ESO (representing its member states), NSF (USA) and NINS (Japan), together with NRC (Canada), MOST and ASIAA (Taiwan), and KASI (Republic of Korea), in cooperation with the Republic of Chile. The Joint ALMA Observatory is operated by ESO, AUI/NRAO and NAOJ.

References

Agúndez, M., Cernicharo, J., Guélin, M. 2007, ApJ, 662, L91
 Anders, E. & Grevesse, N. 1989, GeCoA, 53, 197
 Asplund, M., Grevesse, N., Sauval, A., Jacques, S., P. 2009, ARA&A, 47, 481
 Bachiller, R. 1996, ARA&A, 34, 111
 Bailleux, S., Bogey, M., Demuyneck, C., Liu, Y., Walters, A. 2002, J.Mol.Spec., 216, 465
 Barger, C.J. & Garrod, R.T. 2020, ApJ, 888, 38
 Belloche, A., Müller, H.S.P., Menten, K.M. et al. 2013, A&A, 559, A47
 Beltrán, M.T., Cesaroni, R., Rivilla, V.M., et al. 2018, A&A, 615, A141
 Beltrán, M.T., Rivilla, V. M.; Cesaroni, R., et al. 2021, A&A, 648, A100
 Beltrán, M.T., Rivilla, V.M., Cesaroni, R., et al. 2022, A&A, 659, A81
 Bergner, J.B., Burkhardt, A.M.; Öberg, K.L., et al. 2022, ApJ, 927, 7
 Bernal, J.J., Koelemay, L.A., Ziurys, L.M. 2021, ApJ, 906, 55
 Bisschop, S.E., Jørgensen, J.K., van Dishoeck, E.F. et al. 2007, A&A, 465, 913
 Bonfand, M., Belloche, A., Garrod, R.T., et al. 2019, A&A, 628, 27
 Colzi, L., Rivilla, V.M., Beltrán, M.T., et al. 2021, A&A, 653, 129
 De Beck, E., Kamiński, T., Patel, N.A., et al. 2013, A&A, 558, 132

Endres, P., Schlemmer, S., Schilke, P., Stutzki, J., Müller, H.S.P. 2016, J.Mol.Spec., 327, 95
 Fagerbakke, K.M., Haldal, M., Norland, S. 1996, Aquat Microb Ecol, 10, 15
 Fernández-Ruz, M., Jiménez-Serra, I., Aguirre, J. 2023, ApJ, in press,
 Fontani, F., Pascucci, I., Caselli, P., Wyrowski, F., Cesaroni, R., Walmsley, C.M. 2007, A&A, 470, 639
 Fontani, F., Rivilla, V.M., Caselli, P., et al. 2016, ApJ, 822, L30
 Fontani, F., Rivilla, V.M., van der Tak, F.F.S., Mininni, C., Beltrán, M.T., Caselli, P. 2019, MNRAS, 489, 4530
 Fontani, F., Barnes, A.T., Caselli, P., et al. 2021, MNRAS, 503, 4320
 García de la Concepción, J., Puzzarini, C., Barone, V., Jiménez-Serra, I., Roncero, O. 2021, ApJ, 922, 169
 Garrod, R.T., Jin, M., Matis, K.A., Jones, D., Willis, E.R., Herbst, E. 2022, ApJS, 259, 1
 Garrod, R.T. & Herbst, E. 2006, A&A, 457, 927
 Genzel, R. & Stutzki, J. 1989, ARA&A, 27, 41
 Gieser, C., Semenov, D., Beuther, H., et al. 2019, A&A, 631, 142
 Gueth, F., Guilloteau, S., Bachiller, R. 1998, A&A, 333, 287
 Hollenback, D. & McKee, C.F. 1989, ApJ, 342, 306
 Immer, K., Li, J., Quiroga-Núñez, L. H., et al. 2019, A&A, 632, A123
 Jiménez-Serra, I., Martí-Pintado, J., Rodríguez-Franco, A., Martí, S. 2005, ApJ, 627, L121
 Jiménez-Serra, I., Viti, S., Quénard, D., Holdship, J. 2018, ApJ, 862, 128
 Kanata, H., Yamamoto, S., Saito, M. 1988, J.Mol.Spec., 131, 89
 Kawaguchi, K., Saito, S., Hirota, E. 1983, J. Chem. Phys., 79, 629
 Koo B.-C., Lee, Y.-H., Moon, D.-S., et al. 2013, Sci, 342, 1346
 Lefloch, B., Vastel, C., Viti, S., et al. 2016, MNRAS, 462, 3937
 Lodders, K. 2003, ApJ, 591, 1220L
 López-Gallifa, Á., Rivilla, V.M., Beltrán, M.T., et al. 2023, submitted to A&A
 Macía E. 2005, Chem. Soc. Rev., 34, 691
 Martín, S., Martín-Pintado, J., Blanco-Sánchez, C., et al. 2019, A&A, 631, 159
 McGuire, B.A. 2018, ApJS, 239, 17
 McGuire, B.A. 2022, ApJS, 259, 30
 Mininni, C., Fontani, F., Rivilla, V.M., Beltrán, M.T., Caselli, P., Vasyunin, A. 2018, MNRAS, 476, L39
 Mininni, C., Beltrán, M.T., Rivilla, V.M., et al. 2020, A&A, 644, A84
 Mininni, C., Beltrán, M.T., et al. 2023, accepted by A&A
 Pasek, M.A., Gull, M., Herschy, B. 2017, Chem. Geol., 475, 149
 Rivilla, V.M., Fontani, F., Beltrán, M.T., et al. 2016, ApJ, 826, 161
 Rivilla, V.M., Beltrán, M.T., Cesaroni, R. et al. 2017, A&A, 598, A59
 Rivilla, V.M., Jiménez-Serra, I., Zeng, S., et al. 2018, MNRAS, 475, L30
 Rivilla, V.M., Drozdovskaya, M.N., Altwegg, K. et al. 2020, MNRAS, 492, 1180
 Rivilla, V.M., García De La Concepción, J., Jiménez-Serra, I., et al. 2022, FrASS, 9, 9288
 Tychoniec, L., van Dishoeck, E.F., van't Hoff, M.L.R., van Gelder, M.L., Tabone, B. et al. 2021, A&A, 655, A65
 Wakelam V. & Herbst E., 2008, ApJ, 680, 371
 Woosley, S.E. & Weaver, T.A. 1995, Astrophys. J. Suppl. Ser. 101, 181
 Wurmser, S. & Bergner, J.B. 2022, ApJ, 934, 153
 Ziurys, L.M. 1987, ApJ, 321, L81
 Ziurys, L.M., Schmidt, D.R., Bernal, J.J. 2018, ApJ, 856, 169

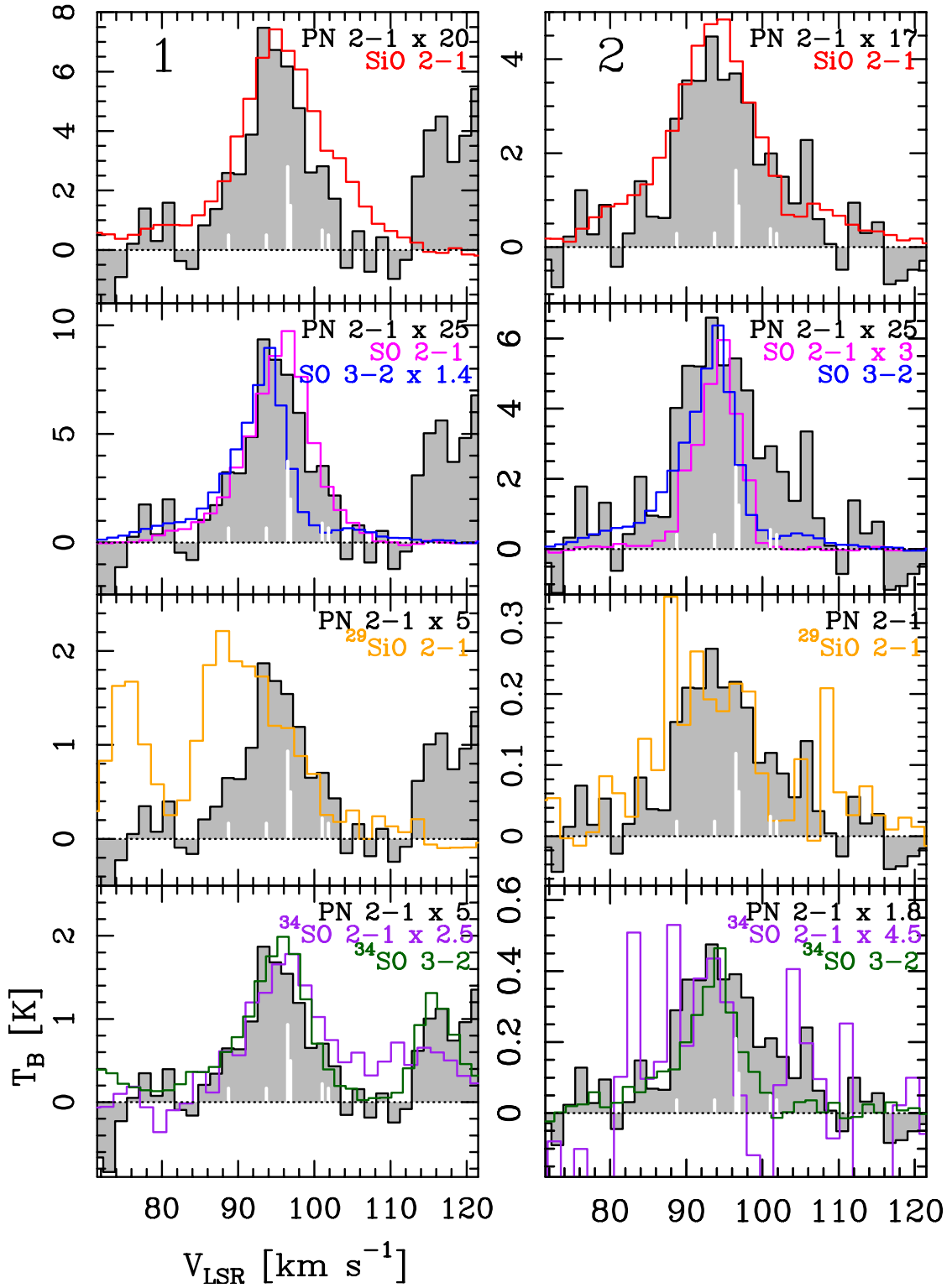


Fig. 8. Spectral comparison between PN, SiO and SO. The PN $J = 2 - 1$ spectra (grey histogram) extracted from regions "1" and "2" in Fig. 1, are superimposed on SiO $J = 2 - 1$ (red histograms), SO $N = 2 - 1(2)$ (magenta histograms), SO $N = 3 - 2$ (blue histograms), $^{29}\text{SiO } J = 2 - 1$ (orange histograms), $^{34}\text{SO } N = 2 - 1(2)$ (purple histograms), and $^{34}\text{SO } N = 3 - 2$ (green histograms) extracted from the same regions. The PN line intensity scale has been appropriately multiplied to perform a consistent spectral comparison with SiO and SO. In each plot, the white vertical bars are the theoretical positions in velocity of the PN $J = 2 - 1$ hyperfine components (Table 1), with the strongest one being at the systemic velocity of 96.5 km s^{-1} .

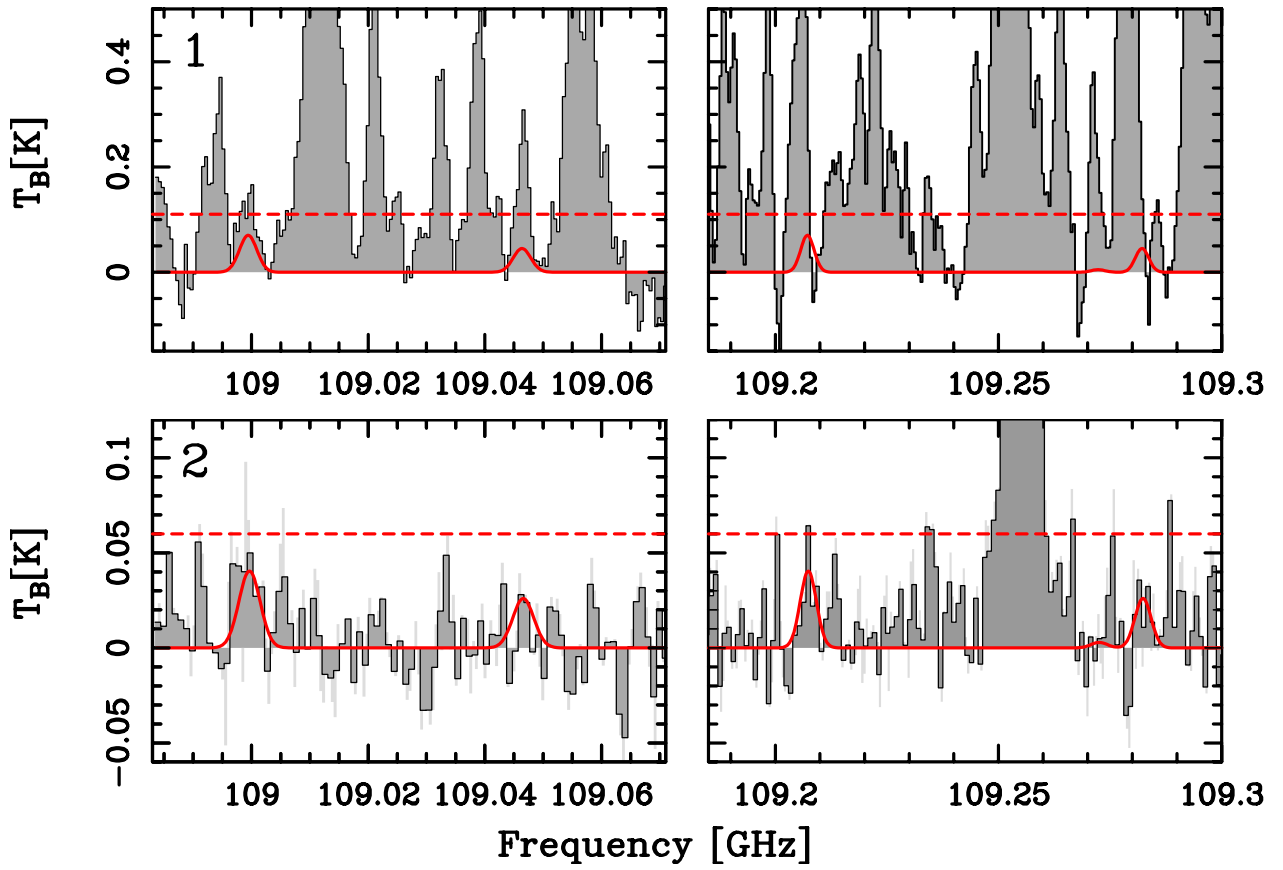


Fig. 9. Spectra containing the PO lines in the GUAPOS observations. *Upper panel:* spectrum extracted towards region "1". The red curve indicates the PO lines fitted according to the best-fit parameters in Table 2 (assuming $T_{\text{ex}}=26$ K). The horizontal red dashed line corresponds to the 3σ rms level. *Lower panel:* same as top panel for region "2", using the fit shown in Table 2 assuming $T_{\text{ex}}=12$ K. The observed spectra at original frequency resolution are shown in light gray, while the spectra smoothed by a factor of 2 are shown in dark gray.

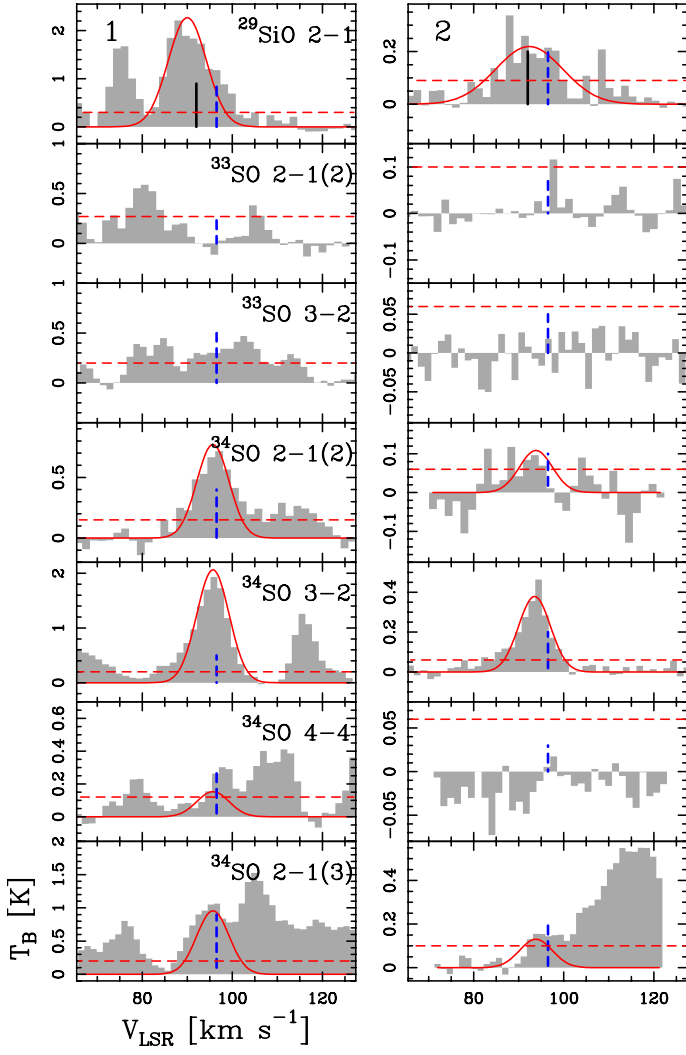


Fig. 10. Same as Fig. 6 for the lines of $^{29}\text{SiO } J = 2-1$, $^{33}\text{SO } N = 2-1(2)$ and $N = 3-2$, and $^{34}\text{SO } N = 2-1(2)$, $N = 3-2$, $N = 4-4$, and $N = 2-1(3)$. The black solid vertical line in the spectrum of $^{29}\text{SiO } J = 2-1$ indicates the expected peak velocity of $\text{C}_2\text{H}_5\text{CN } J_{K_a, K_b} = 11_{2,10} - 11_{1,11}$. In each panel, the horizontal red dashed line shows the 3σ rms level.

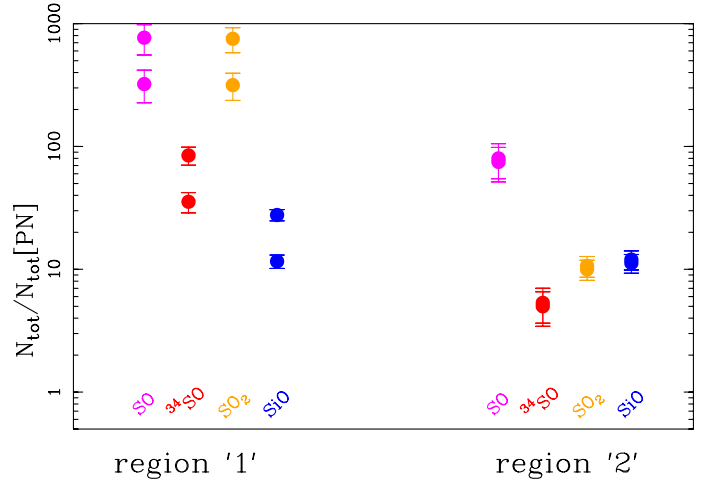


Fig. 11. Column density ratios between molecular species and PN. The different molecules are identified by different colours, and the measurements obtained in region "1" and "2" are separated on the x-axis as indicated. For each molecule, we plot two values of $N_{\text{tot}}/N_{\text{tot}}[\text{PN}]$, which correspond to the two $N_{\text{tot}}[\text{PN}]$ obtained in the T_{ex} velocity interval given in Sect. 3.3.2 (Table 2).